frontiers in Astronomy and Space Sciences

METHODS
published: 30 August 2018
doi: 10.3389/fspas.2018.00025

Understanding the Death of Massive Stars Using an Astrophysical Transients Observatory

Peter W. A. Roming[1], Eddie Baron[2], Amanda J. Bayless[3], Volker Bromm[4], Peter J. Brown[5], Michael W. Davis[3], Anastasia Fialkov[6], Brian Fleming[7], Kevin France[7], Chris L. Fryer[8], Thomas K. Greathouse[3], Jed J. Hancock[9], D. Andrew Howell[10,11], Andrew J. Levan[12], Abraham Loeb[6], Raffaella Margutti[13], Mark L. McConnell[14], Paul T. O'Brien[15], Julian P. Osborne[15], Daniel A. Perley[16], Eric M. Schlegel[17], Rhaana L. C. Starling[15], Nial R. Tanvir[15], Mark Tapley[18], Patrick A. Young[19] and Bing Zhang[20]*

[1] Department of Space Engineering, Southwest Research Institute, San Antonio, TX, United States, [2] Homer L. Dodge Department of Physics and Astronomy, University of Oklahoma, Norman, OK, United States, [3] Department of Space Science, Southwest Research Institute, San Antonio, TX, United States, [4] Department of Astronomy, University of Texas at Austin, Austin, TX, United States, [5] Department of Physics, Texas A&M University, College Station, TX, United States, [6] Harvard-Smithsonian Center for Astrophysics, Institute for Theory and Computation, Cambridge, MA, United States, [7] Laboratory for Atmospheric and Space Physics, University of Colorado Boulder, Boulder, CO, United States, [8] Los Alamos National Laboratory, Center for Nonlinear Studies, Los Alamos, NM, United States, [9] Space Dynamics Laboratory, Utah State University, Logan, UT, United States, [10] Las Cumbres Observatory, Goleta, CA, United States, [11] Department of Physics, University of California, Santa Barbara, Santa Barbara, CA, United States, [12] Astronomy & Astrophysics Group, Department of Physics, University of Warwick, Coventry, United Kingdom, [13] Department of Physics and Astronomy, Weinberg College of Arts & Sciences, Northwestern University, Evanston, IL, United States, [14] Department of Earth Oceans and Space, Southwest Research Institute, Durham, NH, United States, [15] Department of Physics and Astronomy, University of Leicester, Leicester, United Kingdom, [16] Dark Cosmology Centre, Niels Bohr Institute, University of Copenhagen, Copenhagen, Denmark, [17] Physics & Astronomy, University of Texas at San Antonio, San Antonio, TX, United States, [18] Department of Spacecraft Development, Southwest Research Institute, San Antonio, TX, United States, [19] School of Earth and Space Exploration, Arizona State University, Tempe, AZ, United States, [20] Astronomy & Astrophysics Group, Department of Physics and Astronomy, University of Nevada, Las Vegas, NV, United States

OPEN ACCESS

Edited by:
Lee Samuel Finn, Pennsylvania State University, United States

Reviewed by:
Paul Kuin, University College London, United Kingdom
Karelle Siellez, Georgia Institute of Technology, United States

***Correspondence:**
Peter W. A. Roming
proming@swri.edu

Specialty section:
This article was submitted to Cosmology, a section of the journal Frontiers in Astronomy and Space Sciences

Received: *31 October 2017*
Accepted: *23 July 2018*
Published: *30 August 2018*

Citation:
Roming PWA, Baron E, Bayless AJ, Bromm V, Brown PJ, Davis MW, Fialkov A, Fleming B, France K, Fryer CL, Greathouse TK, Hancock JJ, Howell DA, Levan AJ, Loeb A, Margutti R, McConnell ML, O'Brien PT, Osborne JP, Perley DA, Schlegel EM, Starling RLC, Tanvir NR, Tapley M, Young PA and Zhang B (2018) Understanding the Death of Massive Stars Using an Astrophysical Transients Observatory. Front. Astron. Space Sci. 5:25. doi: 10.3389/fspas.2018.00025

The death of massive stars, manifested as gamma-ray bursts and core-collapse supernovae, critically influence how the universe formed and evolves. Despite their fundamental importance, our understanding of these enigmatic objects is severely limited. We have performed a concept study of an Astrophysical Transient Observatory (ATO) that will rapidly facilitate an expansion of our understanding of these objects. ATO combines a very wide-field X-ray telescope, a near-infrared telescope, a multi-mode ultraviolet instrument, and a rapidly slewing spacecraft to realize two primary goals: (1) characterize the highest-redshift massive stars and their environments, and (2) constrain the poorly understood explosion mechanism of massive stars. The goals are met by observing the first massive stars to explode as gamma-ray bursts and to probe their environments, and by observing the shock breakout of core-collapse supernovae to measure the outer envelope parameters of massive stars. Additionally, ATO will observe the shock breakout of Type Ia supernovae and their shock interaction with a companion,

electromagnetic counterparts to gravitational wave sources, kilonovae, tidal disruption events, cataclysmic variables, X-ray transients, flares from exoplanet host stars, and the escape of ionizing radiation from star-forming galaxies. A description of the ATO instruments, the mission simulation, and technology readiness level is provided.

Keywords: gamma-ray bursts, core-collapse supernovae, death of massive stars, astrophysical instrumentation, astrophysical observatory

INTRODUCTION

The death of massive stars is a fundamental process in the shaping of the universe. The first massive stars are considered a significant contributor to reionization and the dispersal of the first metals. These first stars also form the seeds for the formation of supermassive black holes (e.g., Johnson et al., 2012; Whalen and Fryer, 2012). Later generations continue the production and dissemination of heavy elements, which shape planets, solar systems, future generations of stars, and galaxies. They form the neutron stars and black holes in the universe, dictating the characteristics and formation rates of X-ray binaries, X-ray bursts, kilonovae, and gravitational wave sources (e.g., Fryer et al., 1999; Belczynski et al., 2014; Dominik et al., 2015; Regimbau et al., 2015; Abbott et al., 2016). Despite their importance, the nature of the first stars, their contribution to reionization, and how massive stars end their lives, is not well-understood. With an eye toward the future to better understand these enigmatic objects, we have performed a concept study of an Astrophysical Transient Observatory (ATO) that will readily tackle these problems.

ATO accomplishes this by combining a very wide-field X-ray telescope (WFXT) for triggering and X-ray follow up; a near-infrared telescope (NIRT; 0.7–2.0 μm) for imaging and spectroscopy (R$\sim$16 and 1,000); a multi-mode ultraviolet instrument (MUVI; 115–350 nm) for imaging and spectroscopy (R$\sim$3,000); with a rapidly-slewing spacecraft. The WFXT is used for localizing gamma-ray bursts (GRBs), shock breakout (SBO) events from core-collapse supernovae (CCSNe), and other X-ray transients (Campana et al., 2006; Soderberg et al., 2008; Modjaz et al., 2009). When a new target is found by the WFXT, the spacecraft rotates $\sim$180° about the anti-sunward vector. The NIRT and MUVI FOV's are centered on the target while slewing WFXT FOV's away from the sun. Data are simultaneously acquired in imaging and coarse-resolution mode for NIRT and in imaging mode for MUVI. Onboard NIRT software determines the target redshift and inserts the low-resolution spectrograph if it is high-z. If low-z, the MUVI centers the UV spectrograph on the location determined from the MUVI image (see section Concept of Operations). In all cases, all three wavelength regimes continue to observe providing the study of a wide range of transient objects in the universe.

In section Science Goals and Objectives, we describe the science goals and objectives of the ATO mission. In section Science Implementation, we outline the necessary instruments and spacecraft required to meet the science objectives. We also discuss the mission simulation performed to determine the success of the mission. In section Technology Readiness Level, we provide an assessment of the technical readiness level of the concept.

SCIENCE GOALS AND OBJECTIVES

Massive stars end their lives as GRBs and CCSNe. Because of their extreme luminosities, GRBs are excellent probes for characterizing the highest redshift massive stars and the environments within which they reside. Similarly, capturing the SBO of CCSNe is a powerful tool for constraining the poorly understood explosion mechanism of these massive stars, which directly affects our understanding of massive star progenitors and their chemical makeup over cosmic time.

Goals

There are two primary science goals that drive the need for ATO. The first is to characterize the highest-redshift massive stars and their environments; the second is to constrain the poorly understood explosion mechanism of massive stars.

Characterize the Highest-Redshift Massive Stars and Their Environments

Approximately one billion years after the Big Bang, the universe completed its final, large-scale phase transition before the present day. Light emitted by the earliest gravitationally-bound structures ionized the gases between galaxies, allowing ultraviolet (UV) photons to propagate freely across distances comparable to the cosmic horizon scale for the first time and completing the reionization of the cosmos. Although massive stars are thought to be significant contributors to reionization (e.g., Alvarez et al., 2006; Ahn et al., 2012; Robertson et al., 2015), our understanding of them is limited. Some key questions about massive stars include: (1) in what environments do they reside and how does the environment change as a function of redshift, (2) how do they die, (3) when and how does the mode of star formation transition from the zero-metallicity Pop III- to Pop II-dominated stars, and (4) what is the initial mass function for the early Pop III and Pop II stars. Unfortunately, observations of individual pre-exploded high-z massive stars are beyond the capability of the James Webb Space Telescope. Their explosions as GRBs may be the best, if not the only way to study these distant objects (Tanvir and Jakobsson, 2007; Roming et al., 2012; Tanvir et al., 2012). Discovering substantial numbers of GRBs at the highest redshifts with ATO will enable a broad range of studies of the Cosmic Dawn with existing observatories and planned facilities, e.g., James Webb Space Telescope (Gardner et al., 2006), Atacama Large Millimeter/submillimeter Array (Wootten and Thompson,

2009), and Wide Field Infrared Survey Telescope (Spergel et al., 2015).

Constrain the Poorly Understood Explosion Mechanism of Massive Stars

The very first electromagnetic signal in the death of massive stars is the supernova (SN) SBO, which is strongly manifested in the soft X-ray and extreme-UV regimes (e.g., Falk, 1978; Klein and Chevalier, 1978). To date, observing this SBO event has been extremely difficult to probe at high energies so that the SBO phenomenon is largely unexplored observationally. Currently, the most fruitful SBO discovery was in fact a serendipitous one (e.g., Soderberg et al., 2008). High signal-to-noise spectra within minutes after the SBO event will uncover the true nature of the physics behind these events, an area that is still poorly understood. The properties of the SBO—such as temperature, energy, and photon diffusion time (Matzner and McKee, 1999)—provide a powerful way of exploring the photosphere of the star and constraining the SN progenitor. These spectra are superb probes of: stellar radii, which are key in eliminating major uncertainties in binary population synthesis models (e.g., linking the parameters of the explosion directly to the properties of the progenitor star and determining the nature of the remnant); stellar mass-loss that reveals the quantity of mass lost for different stars, ultimately determining the remnant mass distribution; and stellar mixing, crucial for removing major uncertainty in stellar evolution and supernovae (SNe), including nucleosynthesis and galactic chemical evolution. Detection of SBOs also provides an alert to observers of a new SN immediately after core collapse. ATO will be a powerful tool for probing SBO events and in enabling a nearly bolometric study of CCSNe development with existing and planned facilities, such as the Large Synoptic Survey Telescope. In particular, essentially every Large Synoptic Survey Telescope transient will have an X-ray measurement at multiple times, thus by stacking X-ray data we can search for weak SBOs (or place limits on the time of the event).

Objectives

Two primary mission objectives flow from the primary science goals. The first is to observe the first massive stars to explode as GRBs and to probe their environments and the second is to observe the SBO of CCSNe to measure the outer envelope parameters of massive stars. In addition to the primary objectives, many other astrophysical transient events will be observed.

Observe the First Massive Stars to Explode as GRBs and Probe Their Environments

The first stars are likely massive (e.g., Bromm, 2013) and some will end their lives as GRBs (e.g., Ioka et al., 2012). Spectra of corresponding afterglows reveal the imprint of absorption lines that allow determination of the metallicity and ionization state of intervening material along the line of sight, in their host galaxy and across most of the history of the universe. ATO-discovered bursts, with their known near-IR brightness and redshift, will be ready targets for deep spectroscopic observations from NIRT and large telescopes. These spectra will reveal the history of reionization, including variations along different lines of sight; the escape fraction of ionizing radiation from high-z star-forming regions (e.g., Tanvir et al., 2012), a critical and very poorly constrained variable in reionization models; and metal enrichment processes in the early universe.

Each sufficiently high signal-to-noise spectrum of a $z \geq 5$ afterglow provides a point estimate of the HI fraction in the intergalactic medium at the burst redshift, x$HI(z)$. GRB afterglows are uniquely valuable targets for such studies, as they have featureless, synchrotron power-law spectra, allowing the signatures of absorption to be readily identified. To date, only three bursts (GRBs 050904, 130606A, and 140515A) have yielded spectra of sufficient quality to constrain x$HI(z)$ (Totani et al., 2006; Chornock et al., 2013; Hartoog et al., 2015). Knowing which bursts are both near-IR bright and high-z will dramatically increase the yield of high quality spectra for ATO bursts. Afterglow spectroscopy will be critical for inferring the escape fraction of photons from regions of high-z star formation, and in determining the elemental abundances in the host galaxy. Collection of a few hundred burst spectra over a range of redshifts will trace the evolution of metal enrichment over cosmic time.

To maximize the number and discovery efficiency of high-z GRBs, in our study we have chosen eight wide-field imaging Lobster-modules to make up the WFXT, which operate over the 0.3–5 keV band, covering a 1.95 sr field-of-view (FOV) with a typical sensitivity of 2.7 mCrab (30 s integration at 5σ). Experience from the Neil Gehrels *Swift* Observatory (Gehrels et al., 2004; hereafter *Swift*) has shown that GRB properties can confidently be extrapolated into the X-ray band (Evans et al., 2010), with benefits of much lower instrument mass and a greater sensitivity to high-redshift[1].

The critical advance we propose is to immediately follow up WFXT triggers with coarse-resolution (R∼16) near-IR spectroscopy (see **Figure 1**), used to rapidly determine the redshift early enough to efficiently trigger ATO, ground, or other follow-ups across the electromagnetic spectrum. WFXT arcminute positioning will be followed by real time observations by the NIRT featuring simultaneous direct imaging and R∼16 spectroscopy. All GRBs show a break at the redshifted Lyα transition ($\lambda = 0.73\,\mu$m at $z = 5$; $\lambda = 1.95\,\mu$m at $z = 15$), which results from absorption by HI in the host galaxy and intervening intergalactic medium. NIRT rapid response measurements of this break will yield <10% uncertainty in the redshift. Obtaining these redshifts is a crucial step and will prevent any high-z GRBs from being missed due to lack of near-IR follow-up. Bright afterglows determined to be high-z are immediately followed with the NIRT low-resolution (R∼1,000) spectrograph to probe the environment of the GRBs with similar resolution as that used for GRBs 050904, 130606A, and 140515A.

From ATO's measurement of the high-z GRB distribution we will determine the contribution of UV light from the first stars as a source of photons for reionization, and we will test whether a population of zero-metallicity Pop III stars contributes to the GRB rate at high-z (Bromm and Loeb, 2006). Each burst from high-z will be evaluated for indications that it resulted from

[1]Note *Swift's* lower energy bandpass (15–150 keV) discovered GRBs at a mean z∼2.2 (Jakobsson et al., 2012) vs. z∼1 for previous GRB missions.

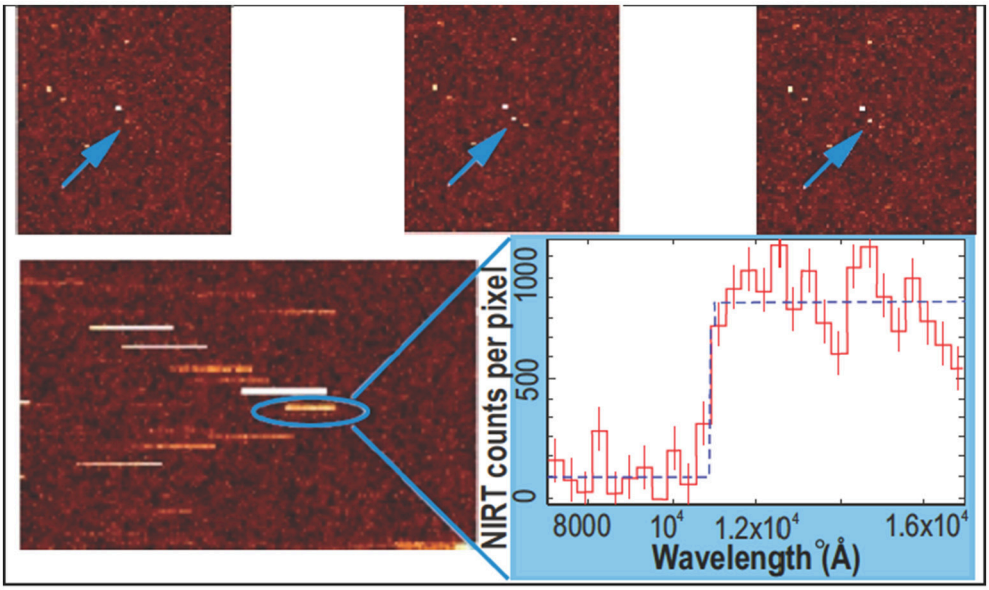

FIGURE 1 | ATO-NIRT images will identify young, variable afterglows (upper 3 images), and objective prism exposures (lower images) will yield redshifts via Ly-break at $z \geq 5$. Once high-z is ascertained, R∼1,000 NIRT spectra will be taken.

TABLE 1 | ATO GRBs over 5 years.

Redshift	No. of ATO GRBs	Total GRBs from *Swift*
$z \geq 5$	282	15
$z \geq 6$	150	7
$z \geq 7$	80	4
$z \geq 8$	42	2
$z \geq 9$	21	1
$z \geq 10$	9	0
$z \geq 11$	2	0
$z \geq 12$	2	0
$z \geq 13$	1	0

a Pop III progenitor (Mészáros and Rees, 2010). Detecting a highly energetic ($E_{iso} > 10^{55}$ erg), long-duration [$t_{(90)} > 500$ s] burst, from high-z ($z > 8$), will make it a strong candidate for a Pop III origin. Should NIRT spectroscopic or a ground-based observation determine very low metallicity, it will be a strong case for the first definitive detection of a Pop III star.

From the WFXT sensitivity, bandpass, and FOV, convolved with a model of GRBs based on *Swift* data, we conservatively project (as the mean of a Poisson process) detection of 282 bursts with $z \geq 5$ (**Table 1**; see Burrows et al., 2012). While *Swift,* according to current models, detects $z > 5$ GRBs at 16% of this rate, the redshifts of the *Swift* bursts are usually unknown, and the bursts' utility for environmental studies unrealized, because sufficient rapid-response near-IR spectroscopy has not been regularly achieved. Over 13 years of effort, only 15 *Swift* GRBs have $z > 5$, with seven confirmed at $z > 6$. The projected redshift distribution of GRBs detected by ATO is given in **Table 1**.

Observe the SBO of CCSNe to Measure the Outer Envelope Parameters

When a CCSNe explodes, it pushes a shock wave through the star until it reaches the outer layers. At the point of SBO the outer layers of the star radiate as a hot pseudo-blackbody, with a peak flux in the far-UV (FUV) or soft X-ray energy range. As the star expands, the escaping emission comes from progressively deeper layers. By the time the SN expands enough for its optical light to be detected, much information about the progenitor star and its environment conditions are lost. Because of high opacities from iron-peak elements, UV light observed in SNe come from a much higher level in the ejecta. Observing the earliest UV light from SNe contains important information on progenitor star sizes and compositions. Tying specific progenitor stars to the resultant explosions is an important goal of stellar evolution studies.

Figure 2 shows broadband light curves for a range of Type II SN using a one-temperature light-curve code (de la Rosa et al., 2016). In these models, we vary a wide range of SN characteristics. With just the light-curve from the primary peak, it is often difficult to distinguish the dominant characteristics. Spectra at late times can provide some information, particularly about the kinetic energy of the explosion. But the breakout emission provides crucial additional constraints, especially on the density profile, stellar radius, and progenitor size. However, with only one breakout observation from a "normal" SN, astronomers have not been able to take advantage of this constraint. By increasing this number 100-fold, this diagnostic will revolutionize our understanding of SNe.

Although some basic trends exist between photospheric radius and breakout peak duration, these results depend upon a number of assumptions about the shock structure (temperature, density) and nature of the emission (thermal vs. nonthermal).

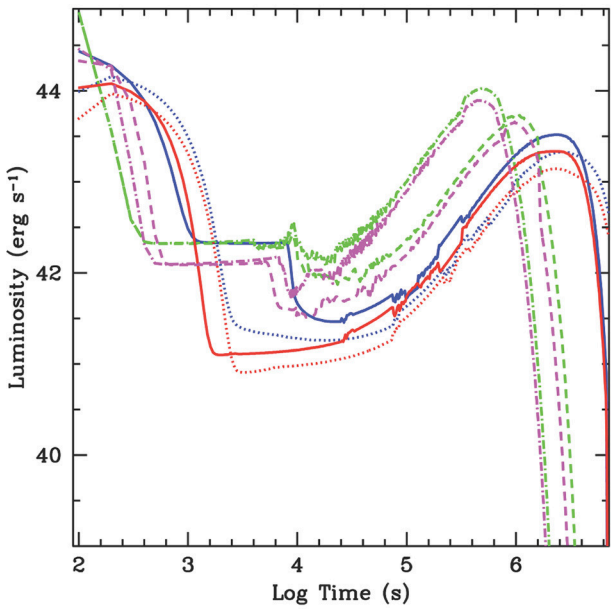

FIGURE 2 | Broadband (115–180 nm) light curves for a range of SN explosions. In the models, we vary initial stellar radius (red and magenta = 10^{12} cm, blue and green = 10^{13} cm), ejecta mass (dotted = $8M_{\odot}$, all others = $4M_{\odot}$), explosion energy (dot-dashed = 6×10^{51} erg, all others = 10^{51} erg), and density profile ($\rho = r^{-\alpha}$; dashed for $\alpha = 2.5$, all others for $\alpha = 0$). All of these factors alter light-curves and with limited data from the primary peak, it is difficult to distinguish these. ATO would disentangle these differences.

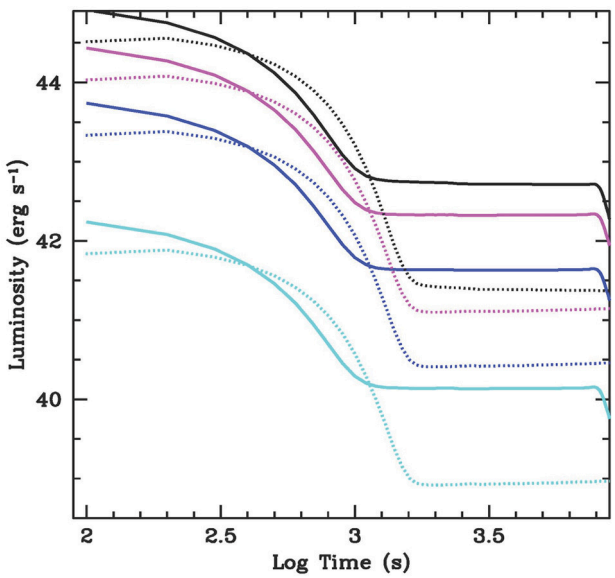

FIGURE 3 | X-ray (black), 115–180 nm (magenta), 200–350 nm (blue), and V-band (cyan) early luminosities as a function of time for two SN explosions whose only difference lie in their radii: 10^{12} cm (dotted), 10^{13} cm (solid). ATO would easily capture this early emission and not only distinguish different radii, but pin down breakout temperatures, which are important for understanding the entire lightcurve.

Observations in both X-ray and UV, allow us to constrain the SN engine. **Figure 3** illustrates X-ray and UV lightcurves, assuming thermal emission and fully ionized atoms where electron scattering dominates the opacity. MUVI spectroscopic observations will also provide constraints on the metallicity.

Table 2 shows a projected detection of 194 SBO events over an ATO five-year mission period. This projection was calculated from the WFXT sensitivity, bandpass, and FOV, convolved with a model of CCSNe based on *Swift* data. As a comparison, over a twelve-year period, *Swift* has detected only two SBO events in X-rays, a critical wavelength for uncovering these events. In addition, only 3–5 UV/optical flashes from SBO events have been detected by the Galaxy Evolution Explorer (Gezari et al., 2008) and *Kepler*[2] (Garnavich et al., 2016). The expected distribution of CCSNe SBO progenitors detected by ATO is also given in **Table 2**.

TABLE 2 | ATO CCSNe SBO over 5 years.

Progenitor	No. of SBOs
Wolf-Rayet (WR)	44
Blue Supergiant (BSG)	4
Red Supergiant (RSG)	126
Other	20
Total	194

Other Transient Astrophysics

A natural byproduct of monitoring a large fraction of the sky for CCSNe SBO events and high-z GRBs is the discovery and monitoring of numerous transients and other sources in the X-ray, UV, and near-IR. Some of these sources include the SBO of Type Ia SNe and their shock interaction with a companion, electromagnetic counterparts to gravitational wave sources (e.g., kilonoavae), tidal disruption events, cataclysmic variables, X-ray transients, flaring from exoplanet host stars, and ionizing radiation escape from star-forming galaxies. Here we briefly discuss some of these science cases.

Type Ia SNe SBOs and shock interactions

Even though we do not understand the full progenitor systems or the explosion process, thermonuclear Type Ia SNe are important cosmological tools for measuring the expansion of the universe. Characterizing the Type Ia SNe explosion mechanism and progenitor system is important in understanding how the explosions and observables might change over the timeframes we use them as standard candles. A sensitive, wide-field X-ray survey could detect the SBO from a detonation (Höflich and Schaefer, 2009; Piro et al., 2010) or the interaction with a companion (Kasen, 2010), while prompt UV follow-up can constrain the size of the white dwarf at the time of the SBO (Piro et al., 2010) and the separation/size of the companion star (Kasen, 2010). Based on models by Kasen (2010), we carried out a rigorous simulation

[2]We note the *Kepler* SBOs are barely inflections on the rising light curve, demonstrating that capturing early SNe with optical telescopes still doesn't yield a clear SBO event. The signal is orders-of-magnitude greater in the UV.

of the WFXT and MUVI performance. From our simulations, we determined that 72 and 16 shock interactions will be seen with the WFXT and MUVI, respectively, over a 5-year mission.

Electromagnetic counterparts to gravitational wave sources

A fraction of gravitational wave sources will be the merger of two neutron stars or a neutron star and a black hole (e.g., kilonovae) and we expect these mergers to also produce electromagnetic counterparts. The combined gravitational wave and electromagnetic signals would provide a decisive probe of the maximum neutron star mass, constraining the nuclear equation of state (Fryer et al., 2015). The concurrent detection in both gravitational and electromagnetic waves of a neutron star merger (Abbott et al., 2017; Chornock et al., 2017; Evans et al., 2017; Kasliwal et al., 2017; Nicholl et al., 2017; Pian et al., 2017; Smartt et al., 2017; Tanvir et al., 2017) has both confirmed aspects of our basic kilonova picture while adding several surprises. First and foremost, the observation of a dim GRB, roughly 30 degrees off-axis (Alexander et al., 2017; Haggard et al., 2017; Hallinan et al., 2017; Margutti et al., 2017; Troja et al., 2017), suggests that our current focused model of GRB jets is not complete (Goldstein et al., 2017). Another surprise arose from the long-lived optical transient to this burst. Although most models with limited wind ejecta predicted only a brief (<1 day) period when the optical emission would be bright (see Kasen et al., 2015; Tanaka, 2016; for counter examples), observations of a >2 day optical transient suggests that this wind ejecta is massive (Troja et al., 2017), on par with the more massive models suggested by Metzger (2017). Alternatively, the jet cocoon could produce extended UV/optical emission (Kasliwal et al., 2017). More extensive UV/Optical observations will help distinguish these models. A possible additional X-ray component, associated with gravitational waves, to search for is that associated with an X-ray powered kilonova (Kisaka et al., 2016) or that associated with post-merger supra-massive magnetar (Zhang, 2013; Sun et al., 2017). We note that the fraction of gravitational wave sources is expected to be small (1–2%; Dominik et al., 2015); however, our WFXT is ideally suited for detecting them.

Tidal disruption events

Tidal disruption events, where the strong tidal force around a massive black hole shreds a star, provide a unique probe of accretion physics from the onset, through super-Eddington rates, to switch off, on a timescale of only a few years. They are also a direct route to studying the ubiquity of black holes in the cores of galaxies, including low-mass systems where such diagnostics are very challenging. ATO will locate lower luminosity thermal tidal disruption events throughout the local universe, finding them at much earlier times than has been typical to date. It could also detect the most luminous tidal disruption events that exhibit relativistic jets, out to $z \sim 4$–6 (e.g., Fialkov and Loeb, 2017), directly probing the frequency of black holes in galaxies where quasars begin to become extremely rare. Since tidal disruption events might be one of the most powerful signposts of the first supermassive black holes, we can use the measured maximum redshifts of tidal disruption events vs. Pop III GRBs to infer the growth of black holes from stellar mass seeds to supermassive systems.

Cataclysmic variables

ATO will transform the study of accreting white dwarf systems. The unique combination of soft X-ray sensitivity and huge instantaneous FOV is ideally matched to the multiple-timescale and highly variable nature of CV emission, which is typically characterized by temperatures of a few keV or lower. ATO's high cadence X-ray monitoring will provide an unprecedented view of white dwarf accretion through all its states and it will be especially capable in discovering new outbursts of classical novae and AM CVn stars. Some classical novae, AM CVn, and steady "super-soft" X-ray sources are considered good candidates for the currently unknown progenitors of Type Ia SNe (Wang and Han, 2012; Maoz et al., 2014); understanding these is vital in further constraining the acceleration of the universe. While X-rays from cataclysmic variables tell us about the white dwarf and its immediate environment, MUVI and NIRT diagnose the accretion disk and secondary star. Consequently, ATO provides a complete view of the whole system.

Flares from exoplanet host stars

The planetary effective surface temperature alone is insufficient to accurately interpret biosignature gases when they are observed in the coming decades. The UV stellar spectrum drives and regulates the upper atmospheric heating and chemistry on Earth-like planets, is critical to the definition and interpretation of biosignature gases (e.g., Seager et al., 2013), and may even produce false-positives in our search for biologic activity (Hu et al., 2012; Tian et al., 2014; Harman et al., 2015). The high-throughput of the MUVI UV spectrograph will allow for efficient monitoring of a sample of low-mass exoplanet host stars to better characterize how their high-energy irradiance spectra and strong flare activity (e.g., **Figure 4**) impact atmospheric chemistry and stability on potentially habitable planets (e.g., Spake et al., 2018). Stellar spot cycles can be monitored as spots cause a decrease in IR emission, but are also associated with an overall UV increase in late-type stars. Interpolation between ATO X-ray and FUV data will provide strong constraints on extreme-UV measurements, which are the biggest contributors to atmospheric photochemistry and atmosphere loss (e.g., Shkolnik and Barman, 2014).

Escape of ionizing radiation from star-forming galaxies

The current dominant paradigm for the hydrogen Epoch of Reionization requires that hot stars in galaxies provide most of the photons to re-ionize the universe. However, the mechanism by which ionizing photons ($\lambda_{rest} < 912$ Å) escape from galaxies is not understood. MUVI will enable sensitive surveys of ionizing radiation escaping from a sample of low-redshift ($z < 0.4$) star-forming galaxies to quantify the fraction of ionizing radiation that escapes into the intergalactic medium. In addition, the broad spectroscopic bandpass and narrow-band imaging capability of MUVI will enable searches for ionizing radiation escape beyond the local universe ($z \sim 0.5$–2). The FUV and near-UV (NUV) imaging modes will allow us to follow-up these targets

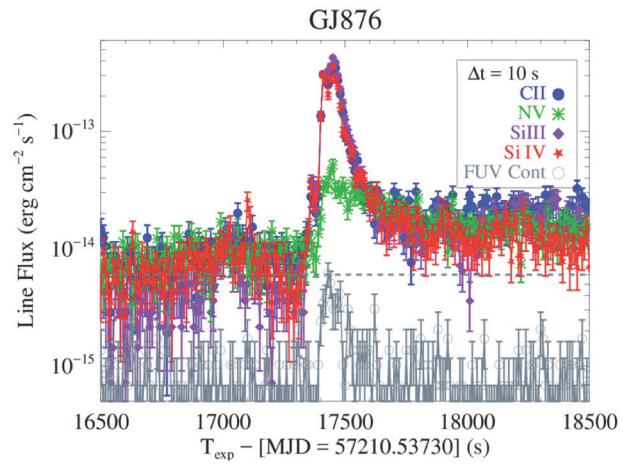

FIGURE 4 | FUV flare on the "optically inactive" M dwarf GJ 876, illustrating the importance of time-resolved UV spectra of exoplanet host stars [HST-COS data, binned to 10 s intervals; adapted from France et al. (2016)]. ATO would capture flares on a *daily* basis.

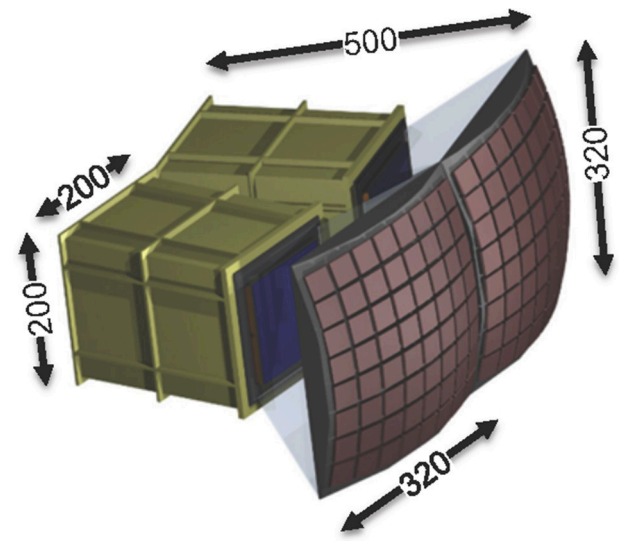

FIGURE 5 | Two of eight ATO-WFXT modules for localizing SBO events and high-*z* GRBs. The dimensions provided are in mm.

to characterize the galactic environments that are favorable for ionizing escape—a local study that will shed light on how ionizing photons escaped from the first galaxies and initiated the Epoch of Reionization. The long bandpass and imaging modes will also allow both imaging-based detection of potential Lyman Continuum emitters at z∼0.6–2, as well as the spectroscopic follow-up for a broad and largely unexplored redshift range.

SCIENCE IMPLEMENTATION

To address the science of high-*z* massive stars, ATO requires GRB detection and afterglow instruments that are particularly sensitive to high-*z* GRBs. For GRB detections at high-*z*, the optimal instrument is a soft X-ray WFXT rather than one tuned for the harder X-ray or gamma-rays (cf. Burrows et al., 2012). Afterglow follow-up requires a NIRT capable of spectroscopy to capture the afterglow at its brightest and maximize the spectral signal-to-noise.

Tackling the SBO science question necessitates detection and follow-up spectroscopy of SNe SBO events. As with GRBs, because of their paucity, detecting breakout events requires a wide FOV instrument such as WFXT. For post-SBO follow-up, a FUV telescope capable of spectroscopy is required for capturing strong key diagnostic lines.

A near-geostationary orbit with telescopes pointed anti-sun is ideally suited for ATO. The WFXT will continuously monitor the sky for GRB and SBO events, while the NIRT and MUVI observe formerly triggered events or ancillary science targets. When the WFXT triggers an event, the spacecraft rapidly slews to the target allowing the co-aligned NIRT and MUVI to begin immediate observations. Public rapid notifications of the target location, brightness, and redshift are sent to other ground- and space-based facilities.

Instruments

Wide-Field X-Ray Telescope

Overview

The ATO WFXT comprises eight modules. Each module is a wide-field lobster eye telescope using the optical principle first described by Angel (1979); **Figure 5** shows a pair of modules. The optics aperture is formed by an array of square pore micro channel plates (MCPs) mounted on a spherical frame. The modules are kept thermally stable. **Table 3** summarizes the anticipated module characteristics. The mechanical envelope of a module is illustrated in **Figure 5**.

Module focal planes are a spherical surface of 300 mm radius of curvature situated a distance of 300 mm from the optics aperture (the focal length). The detectors for each module comprise a 2 × 2 array of large format charge coupled devices (CCDs), which are tilted to match the local tangent to the spherical focal surface. The CCDs are back-illuminated devices operated in a non-inverted mode, cooled below 210 K with a bonded multi-stage thermoelectric cooler, and connected to a high responsively output circuit to ensure good X-ray resolution.

Performance

The imaging area of the CCDs sets the FOV of each module. Using the CCD dimensions, focal length of the telescope, and allowing for the CCD frame store gives an active area of 15.5 × 12.92 sq-deg. The FOV of each module is provided by 4 CCDs giving 801 sq-deg. Thus, a complement of eight WFXT modules has a total non-overlapping FOV of 6,408 sq-deg (1.95 sr).

As measured by similar systems, the full-width-half-max is 4.5 arcmin with all of the true-focus flux contained in a 10-arcmin-diameter beam. Depending on the count rate and integration time, the positional accuracy ranges from 10 to 105 arcsec. To determine the sensitivity of WFXT, we use ROentgen SATellite All-sky Survey data to estimate the count rate expected from point sources and the diffuse sky (Galactic and cosmic). Using

TABLE 3 | WFXT module (1 of 8) properties.

Characteristic	Value
Energy band (keV)	0.3–5
Telescope type	Lobster
Optics aperture (mm^2)	320 × 320
Optics configuration	8 × 8 sq-pore MCPs
MCP size (mm^2)	40 × 40
Focal length (mm)	300
Focal plane shape	Spherical
Focal plane detectors	CCD array
Size of each CCD (mm^2)	81.2 × 81.2
Pixel size (μm)	18
Pixel number	4,510 × 4,510
Number of CCDs	4
Field of view (sq-deg)	801
Positional accuracy (arcsec; best, worst)	10, 105
Sensitivity over 0.3–5 keV in 1,500 s (erg cm^{-2} s^{-1})	3.2×10^{-11}
FWHM resolution, 2 s exp, 1.8 keV, at 210 K (eV)	<100
Power [W]	28
Mass [kg]	30

the average background rate and a false detection probability of 1.0×10^{-10}, the sensitivity to transient sources is plotted as a function of integration time (from 1 to 3.6×10^6 s). We find the sensitivity for a typical ATO exposure time of 1,500 s is 3.2×10^{-11} erg cm^{-2} s^{-1} (see **Table 3**). There is not a brightness limit on the instruments. A very bright X-ray source (e.g., Sco X-1) will saturate the CCD pixels in WFXT, but not affect the rest of the FOV observations. If the source is spread across many pixels (e.g., Crab Nebula) it will not saturate the CCD. MUVI will use the latest UV detectors, which do not have a gain sag issue, but do have electronic dead time. The current detectors have a dead time of ∼1 μs, causing a 9% loss on the count rate at a readout of 100 kHz. Thus, there will not be damage to the detector passing a bright source, but there will be inaccuracies in the count rate that will need to be calibrated.

Trigger algorithm

We use a fast two-stage process that exploits the cruciform structure of the point spread function for maximum sensitivity avoiding the need for computationally expensive 2-D cross-correlation (Osborne et al., 2013). Positions of all transients found must be cross-correlated with known source catalogs, e.g., ROentgen SATellite All-sky Survey, flare stars, *Swift* Burst Alert Telescope (Barthelmy et al., 2005) catalog etc. Any position that does not match a known position must be passed to the spacecraft as a potential trigger position. As this is a focusing instrument, there is not a background flux over short exposures (unlike a coded mask instrument). Thus, we can trigger over the entire integration time with a typical trigger duration of 1 s and up.

Near-Infrared Telescope

The NIRT consists of a Ritchey-Chrétien (R-C) telescope that feeds a 0.7–2.0 μm imaging and spectroscopy system (**Figure 6**). The telescope is a 0.55-m diameter primary operating a focal ratio of f/6.25 and has a 36 × 36 $arcmin^2$ FOV. Three optical trains follow the R-C telescope: an imaging, coarse-resolution, and low-resolution train. Ten percent of the light is deflected into the imaging train by an amplitude beam splitter. The remaining 90% is reflected into either a coarse-resolution direct-view prism spectrometer ($\lambda/\Delta\lambda \sim 16$) or a low-resolution grating spectrometer ($\lambda/\Delta\lambda \sim 1{,}000$) by a two-position mirror.

Dichroic cube beam splitters in both the coarse- and low-resolution optical trains split the passband into a short-wavelength channel and a long wavelength channel. Cube designs are used for both beam splitters to avoid the astigmatism associated with tilted plates in focused beams. Achromatic CaF_2-SiO_2 field corrector lenses located near the focal planes are used. Coatings on the SiO_2 element of the field correctors block the UV fluorescence associated with CaF_2. The secondary mirror is an active fast steering mirror for image stabilization that also provides for focus correction. The aperture stop is at the secondary mirror to prevent the detectors from seeing the inside of the primary mirror baffle tube. The primary and secondary mirrors are 50% light-weighted Zerodur (cf. Döhring et al., 2009).

The NIRT structure consists of a fore optics baffle, fore optics metering structure, aft optics support structure, and spacecraft interface structure, and is made of K13C2U composite to provide a thermally efficient and structurally sound solution for the structure baffles and cover. The cover opens into a sunshade protecting the NIRT fore-optics baffle tube from direct solar illumination. Assuming level 300 particulate contamination, the non-rejected Earth irradiance at the detector is an order of magnitude below the zodiacal background at an Earth limb angle of 15° and a factor of 50 below the zodiacal background at 30°. The thermal emission from the optics is an order-of-magnitude less than the zodiacal light.

The NIRT thermal design uses both active and passive approaches to provide cooling to the required levels. The telescope aperture provides passive radiative cooling for the telescope optics and baffle. Orbital thermal modeling using hot-case end-of-life parameters predicts a 240 K temperature for the telescope optics and baffle. A focal plane operational temperature <100 K is achieved using an active micro-pulse tube cooler. Each of the five NIRT detectors is a 2 k × 2 k Mercury-Cadmium-Telluride H2RG detector (Beletic et al., 2008) with SIDECAR ASICs (e.g., Dorn et al., 2008). The nominal quantum efficiency is ∼0.7. The correlated double sample read noise is <30 e^-/pixel, which is reduced further to <10 e^-/pixel with Fowler sampling. Top-level NIRT properties can be found in **Table 4**.

Multi-Mode Ultra-Violet Telescope

MUVI consists of a R-C telescope that feeds a FUV and NUV imaging and spectroscopy system (**Figure 7**). The telescope is a 1-m diameter primary operating at a focal ratio of f/15. The imaging system will accept light off of a polished flat slitjaw mirror, focusing the beam with a toroidal camera optic and directing the FUV and NUV channels with a steering mirror that directs the light through a filter wheel and onto either the FUV or NUV detector. The FUV channel will be imaged onto a sealed tube, MgF_2 windowed, photon counting MCP

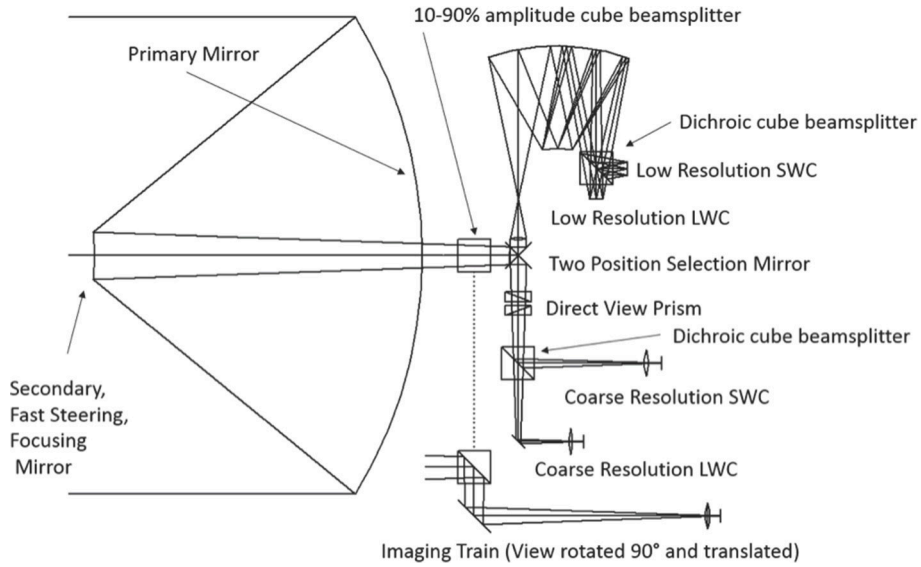

FIGURE 6 | Optical layout of the NIRT showing the imaging (Direct; 0.7–2.0 μm), coarse resolution short-wave (SWC; 0.7–1.35 μm), and long-wave (LWC; 1.35–2.0 μm) channels, and the R∼1,000 spectrograph. This design offers high throughput while providing arcsec-level imaging for GRB localization, rapid redshift determination, and spectroscopic follow-up.

TABLE 4 | NIRT. and MUVI properties.

Characteristic	NIRT	MUVI
Wavelength (nm)	700–2,000	115–350
Telescope type	R-C	R-C
Aperture (m)	0.55	1.0
Focal ratio	f/6.25	f/15
Detectors	H2RG	MCP, CCD
Linear detector size (mm)	37	45/50, 28
Pixel size (μm)	18	12.5, 13.5
No. of mega-pixels	4	13/16, 4
No. of detectors	5	2, 2
Spectral res	∼16 and 1,000	∼3,000
FOV (sq-arcmin)	1,296	100
Positional accuracy (arcsec)	1	1
Angular res (arcsec)	<1	∼1
Power [W]	87	84
Mass [kg]	172	126

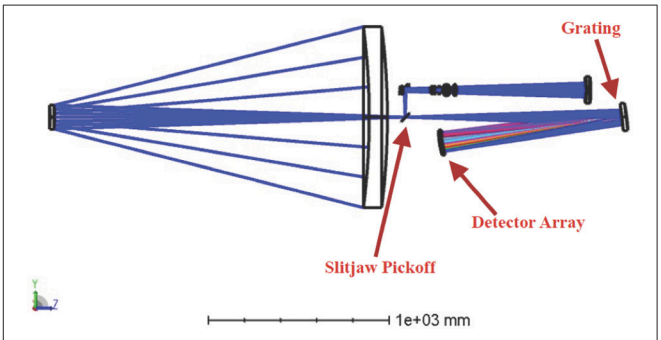

FIGURE 7 | MUVI telescope, spectrograph, and imager design. This design offers high throughput while maintaining low-resolution spectroscopy and ∼arcsecond-level imaging for SN localization, galactic characterization, and light curve follow-up.

while the NUV channel will be focused onto an NUV-optimized CCD. The FUV and NUV spectroscopy channels will be fed through a traditional long-slit aperture and will be dispersed by a toroidally-figured diffraction grating that sends light to the FUV and NUV detector arrays. The FUV and NUV spectral channels are recorded simultaneously on windowed MCP (FUV) and CCD (NUV) detectors, separated by a gap of ∼10 mm.

The primary instrument components are the telescope and imager optics, imaging filters, the diffraction grating, and four detectors. The telescope optics will be fabricated from fused silica substrate and coated with a thin layer of Al+MgF_2 to enhance reflectivity across the UV bandpass (down to the coating edge of 115 nm). The filters are chosen to match existing flight filter sets. The grating is holographically ruled on a toroidal substrate. The FUV detectors will be 45 mm (imaging) and 50 mm (spectroscopy) square cross-delay line anode MCPs, respectively; fairly "standard" space flight detectors. The NUV detectors will be the CCD42-40 NIMO UV-enhanced devices, similar to the NUV-sensitive CCD detector flown on the *New Horizons* mission to Pluto.

The MUVI instrument provides <1 arcsec imaging (spacecraft- and attitude determination and control-limited) over the inner 5 arcmin of the MUVI FOV (∼10 arcmin), which accomodates the primary science goal of localizing and characterizing the galactic regions from which SNe originate.

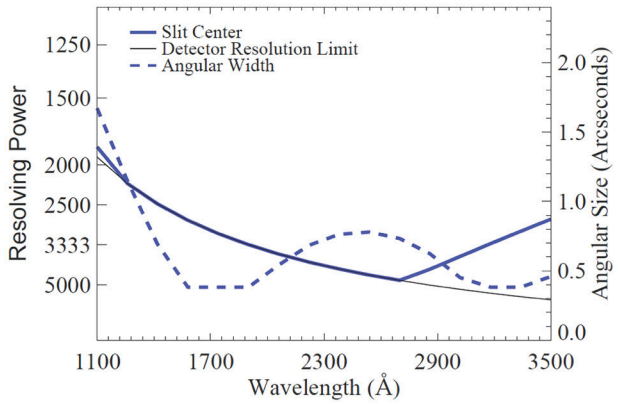

FIGURE 8 | MUVI UV spectral and imaging resolution. The solid curve shows the spectral resolving power and the dashed curve shows the angular resolution of MUVI.

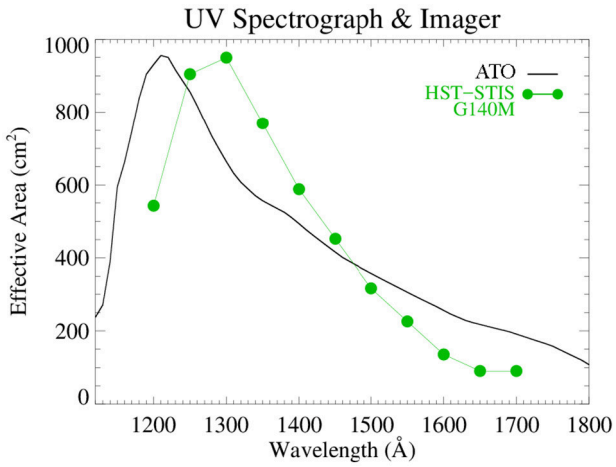

FIGURE 9 | MUVI FUV effective area. Through efficient design and modern componentry, the 1-m system provides comparable performance to the medium-resolution grating mode on HST-STIS (G140M). Note that STIS has higher spectral resolution while MUVI has a factor of ∼15 more spectral bandpass per exposure.

Given that the WFXT localizations will be ≤105 arcsec for ATO-discovered targets, the MUVI FOV provides substantial margin for target localization and will enable almost full-galaxy imaging for SNe erupting in the nearby universe (d < 10 Mpc). The spectrograph provides $R \geq$ 2,000 imaging spectroscopy (through a 5′′ × 10′ long-slit) across the FUV and NUV bandpasses, from 115 to 350 nm. The system works in a long-slit imaging mode, with ∼1 arcsec angular resolution spectral imaging within 5 armin of the center of the slit. **Figure 8** shows the spectral and imaging performance of MUVI across the UV bandpass. The individual FUV (115–180 nm) and NUV (200–350 nm) spectral channels operate simultaneously and provide full FUV+NUV spectral coverage of the SN early-time evolution, with a gap between 180 and 200 nm. Owing to the efficient system design and state-of-the-art componentry, MUVI delivers similar total sensitivity (effective area) as the medium-resolution grating modes on the Hubble Space Telescope—Space Telescope Imaging Spectrograph (**Figure 9**), despite the 6x smaller collecting area. While the G140M mode on the Space Telescope Imaging Spectrograph has higher angular and spectral resolution compared to MUVI, the MUVI FUV spectroscopy modes covers more than 10x the bandpass in each spectrum and more than 10x the imaging spectroscpy FOV. Top-level MUVI properties can be found in **Table 4**.

Spacecraft/Observatory

Requirements and Overview

The spacecraft carries eight WFXT modules to image 1.95 sr of the celestial sphere simultaneously. It also supports the NIRT and MUVI, boresighted with one of the WFXT modules for event localization. Rapid slew rates with a sun-aware slew algorithm and fine guidance control performing at 1 arcsec-s (3 σ) over periods up to 24 h permit speedy acquisition (<120 s from detection to settling) and target separation from galactic core emissions in the host galaxy. All of the instruments, attitude determination and control star trackers, and scalable inertial reference unit mount to a single optical bench to ensure pointing stability during slews, and the entire optical system is protected by an asymmetric sunshade allowing the telescopes to observe up to solar elongation angles as low as 60°. During event observations, the non-co-boresighted WXFT modules are pointed away from the sun at elongation angles >60°, permitting continued imaging over the same 1.95 sr area of sky. A near-geosynchronous orbit (24-h period but with small inclination and eccentricity to avoid occupying a slot in the exact geostationary earth orbit band) permits continual coverage from a single ground station. A low-rate dedicated omnidirectional S-band link carries GRB and SBO alerts to support ground observations and the science data come down over a steerable Ka-band medium-gain antenna at scheduled contact times.

Concept of Operations

Figure 10 depicts the spacecraft layout and shows the co-alignment of instrument FOVs. While searching for new transients, the individual exposures (∼1 s) are coadded. If a new transient is not discovered within our sensitivity limits (coadded time ∼1,500 s), we begin a new image. While monitoring the X-ray sky, we will be observing other targets with MUVI and NIRT. We are using an on-board catalog to compare the new images. When a new target is found by the WFXT, the spacecraft rotates ∼180° about the anti-sunward vector to place the target opposite the WFXT array, then slews to center the NIRT and MUVI FOV's on the target while slewing WFXT FOV's away from the sun. Once the target is in the FOV of NIRT and MUVI, data are simultaneously acquired in imaging and coarse-resolution mode for NIRT and in imaging mode for MUVI. If the onboard NIRT software algorithm determines from the coarse-resolution mode that the target is high-z, the low-resolution spectrograph is placed on the location determined by the NIRT image. Otherwise the MUVI spectrograph is placed on the location determined from the MUVI image by the onboard MUVI software algorithm. We

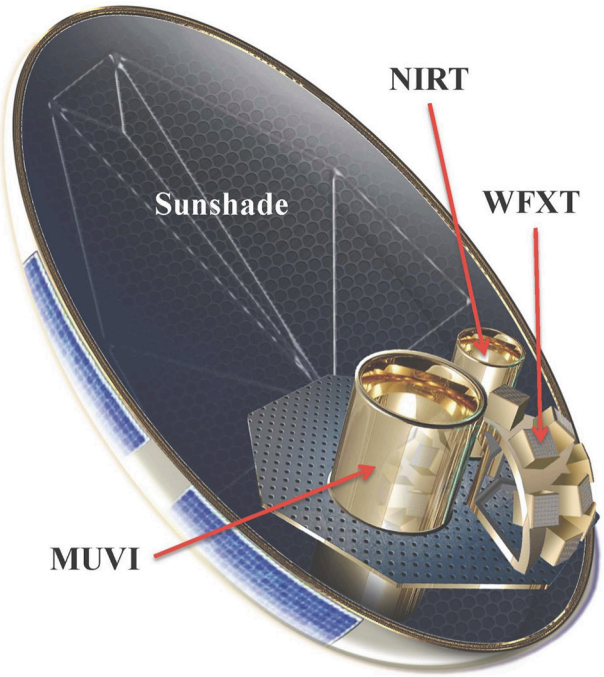

FIGURE 10 | ATO observatory layout. The eight WFXT modules, NIRT, and MUVI are highlighted. The sunshade is also highlighted.

expect the UV flux to be accurate to 1% for a Probe class mission, an improvement over *Swift* UVOT's >5% accuracy (Roming et al., 2009). In all cases, the WFXT modules, including the one boresighted with NIRT and MUVI, continues to observe. On-board calibrations are obtained using bright emission line sources for wavelength calibrations.

Performance

The asymmetrical sunshade and solar array keep the science payload in shadow at all times to provide a very consistent and cold thermal environment, minimizing load on the detector coolers for the WFXT and NIRT. Optical bench and detector electronics equilibrate to a static −50°C isothermal condition, with thermoelectric cooler-driven radiators cooling the NIRT detectors to 100 K. Three Technical University of Denmark μASC star trackers and a scalable inertial reference unit mounted to the optical bench as well as pointing feedback from NIRT provide stare mode pointing stability of 0.7 arcsec-s (3 σ) as measured at the optical bench, meeting the pointing requirement with margin. The 2 m^2 primary solar array provides 600 W (end-of-life) while searching for new transients, easily adequate for thermal control as well as all payload power needs. A secondary array provides at least 420 W for observations down to 45° solar elongation angle. A 20 A-hr Li-Ion battery provides power through maximum eclipse duration. S-band downlink at 2 kbps and uplink at 64 kbps meet requirements for housekeeping, command, and breakout alert data while the 50 Mbps Ka-band downlink carries all science data. An array of 6 Honeywell HR-16 reaction wheels meets the slew time requirement with substantial margin while providing redundancy and fine guidance control. A monopropellant blow-down hydrazine system with 8 thrusters provides momentum dumping and orbit maintenance as well as end-of-mission disposal capability.

We expect a slew rate similar to *Swift* (∼50 deg/min) when a new target is discovered by WFXT. Otherwise, the observatory will be constantly monitoring the X-ray sky while observing other targets waiting for a trigger. We will respond to all triggers within the viewing constrants of the observatory.

Mission Simulations

High-*z* GRBs

To predict ATO burst rates as a function of redshift, we simulated a complete population of GRBs via the luminosity and redshift distributions of Wanderman and Piran (2010), drawing burst redshifts ($0 < z < 30$) and luminosities ($L_{peak} \geq 10^{50}$ erg s^{-1}) from these distributions according to the appropriate all-sky rate. The duration (T_{90}) and spectrum of one of 111 *Swift* Burst Alert Telescope bursts with known redshift are then scaled to the new target redshift and luminosity, used to calculate the flux and integration time (maximum of 2,000 s) for WFXT, and compared to WFXT detection thresholds. The properties of all detected bursts are recorded and form the basis for our predicted redshift distribution. To minimize Poisson uncertainties, the simulation is carried out for an on-orbit period of 10 years, and results then rescaled to the mission duration.

As a result of the simulations, we predict a mean burst detection rate of 1.06 GRBs per week with the WFXT. Overall, we find that a cumulative fraction of 12% for $z = 5$, 6.4% for $z = 6$, 3.4% for $z = 7$, 1.8% for $z = 8$, 0.9% for $z = 9$, 0.4% for $z = 10$, 0.01% for $z = 11$, 0.07% for $z = 12$, 0.03% for $z = 13$, and 0.02% for $z = 14$ of ATO bursts; beyond $z = 15$ the Lyα break redshifts beyond the NIRT bandpass so that a redshift measurement is not assured; 0.07% of WFXT bursts fall beyond this cutoff.

SBO of CCSNe

To predict ATO SBO rates, we carried out a rigorous simulation of the WFXT performance. The SBO simulation uses the SN rate of Strolger et al. (2015) to determine the number of CCSNe available in a 5-year period. Each SN is assigned to a galaxy. The galaxy distribution is determined from the Galaxy Catalog of White et al. (2011), which is complete to 100 Mpc. Using this catalog, we extrapolate the number of galaxies out to 500 Mpc. There is a fall off in the number of detectable sources after 500 Mpc, but we should still detect WR SNe out to 1,000 Mpc. The extrapolated galaxies past 100 Mpc are given a random RA, DEC, and distance. The SNe are then assigned a type and weighted according to Strolger et al. (2015) and Smartt (2009): Red Super Giant (RSG; 59.7% of SNe), Blue Super Giant (BSG; 1%), Wolf-Rayet (WR; 31.34%), or Other (e.g., IIn's; 7.96%).

Each SN was then assigned an X-ray peak luminosity (L_X), peak time (t_{peak}), and light curve shape, based on the ATO team's and Nakar and Sari (2010) models, and constrained to a narrow distribution based on the X-ray SNe 2006aj (Campana et al., 2006) and 2008D (Soderberg et al., 2008; Modjaz et al., 2009). The mean values for L_X and t_{peak} as a function of CCSNe progenitor type are found in **Table 5**. We also assign a random hydrogen

TABLE 5 | Simulation properties.

CCSNe Progenitor	<*logL*>	<t_{peak} (s)>
X-RAY		
RSG	43.0	1,500
BSG	44.0	150
WR	45.0	10
Other	44.0	1,500
UV		
RSG	42.5	1,500
BSG	43.5	150
WR	44.5	100
Other	43.5	1,500

column density (N_H) to each SN based on the distribution in Willingale et al. (2010). The SN luminosity is converted into brightness after attenuation for distance and N_H. We then determine if and for how long the SN is visible in the X-ray based on the sensitivity of the WFXT.

Each SN was then assigned a UV luminosity (L_{UV}), t_{peak}, and light curve shape, based on the ATO team's and Nakar and Sari (2010) models, and constrained by *Swift* UVOT (Roming et al., 2005) observations of CCSNe (Brown et al., 2014; Pritchard et al., 2014). The mean values for L_{UV} and t_{peak} as a function of CCSNe progenitor type are found in **Table 5**. The L_{UV} is then converted into brightness after attenuation for extinction and distance. To calculate extinction, N_H is converted into an E(B-V) value according to the convention of Predehl and Schmitt (1995) and then the total extinction determined using Cardelli et al. (1989), assuming an $R_V = 2.72$ as a worst-case scenario. We then determine if the SN is visible and for how long in the UV using MUVI's sensitivity.

How Mission Meets Science Objectives

High-*z* GRBs

One of the lessons learned from *Swift* is the criticality of co-locating a near-IR afterglow instrument with a prompt burst detector. The primary reason for co-locating the ATO WFXT and NIRT is to ensure prompt observation of the afterglow during its brightest phase, when its redshift can be readily measured. By contrast, approaches that depend on external coordinated near-IR observations, such as *Swift*, have been hit-or-miss. This capability of ATO is thus a significant improvement on current observations.

With ATO, each WFXT detected burst is observed by the NIRT as soon as spacecraft constraints allow. This results in observations within minutes instead of hours/days for most bursts. Extrapolating from the observed properties of three $z > 6$ bursts, we calculate continuum fluxes redward of Lyα after redshifting to $z = 9$ and $z = 12$. We find that in a 610-s coarse spectroscopic segment (which includes integration, Fowler sampling, and dither times), beginning 200 s after the burst, the NIRT provides signal-to-noise per resolution element ranging from 3.0 to 1,310 for these bursts. This is a preliminary estimate which will need future refinement for the mission.

SBO of CCSNe

From the X-ray observations, ATO will be able to measure the SBO for ∼200 SNe, while characterizing the fraction of all SNe with a SBO. The temperature of the shock will cool quickly resulting in a rapid change of the spectral energy distribution peak. This will be followed efficiently by the MUVI FUV spectrograph, as cycling through filters would not provide sufficient simultaneous resolution in time or wavelength. The prompt discovery of these objects and their announcement to ground-based follow-up teams will result in optical observations that are younger than that routinely observed today. They will be able to follow the evolution of the SN as the energy output shifts into the optical. From the time-resolved multi-wavelength data of the SBO curves, we will constrain the radii, ejecta mass, explosion energy, and density profile (Bayless et al., 2017).

TECHNOLOGY READINESS LEVEL

The WFXT is based on lobster-eye grazing incidence technology that has been under development for over two decades (e.g., Fraser et al., 2002) and is slated, or proposed, to fly on numerous missions (e.g., Fraser et al., 2010; Mercier et al., 2014; Raab et al., 2016; Amati et al., 2018). All subsystems of the WFXT are technology readiness level (TRL) ≥6.

The NIRT design is based on flight-proven instruments flown including NEOWISE, Worldview 1&2, WISE, and Geosynchoronous Imaging Fourier Transform Spectrometer (GIFTS). All subsystems of the NIRT are TRL ≥ 6.

The MUVI design builds off of payloads demonstrated on suborbital missions (France et al., 2004; Lupu et al., 2008; Fleming et al., 2013), while all of the optics, coatings, and detectors have a space-flight heritage connections to long-duration NASA missions (including HST/COS), meaning that all components of MUVI are TRL 5–6 or higher.

The capabilities required for the spacecraft are all within the capabilities of current technologies.

CONCLUSION

The motivation behind the ATO concept is to significantly expand our understanding of the death of massive stars, which are key to our understanding of many other aspects of astrophysics. Other observatories have explored components in the death of massive stars, including: *Chandra* and the Nuclear Spectroscopic Telescope Array studying exploded stars in the form of SN remnants (e.g., Park et al., 2002; Lopez et al., 2015); *Swift* and *Fermi* expanding our view of GRBs (e.g., Gehrels and Razzaque, 2013), SNe (e.g., Brown et al., 2015), and other transient phenomena (e.g., Kennea, 2015); the Hubble Space Telescope providing some of the best UV spectra of CCSNe and studies of the environment of GRBs (e.g., Baron et al., 2000); and *Kepler* capturing the SBO of two massive stars in optical light (Garnavich et al., 2016). However, despite the tremendous progress made by these observatories in increasing our understanding of massive stars, no current or planned mission has the capability to move our understanding of high-*z*

massive stars and CCSNe SBO from discovery to exploration. The ATO is designed to progress our understanding of these massive objects into the next phase.

AUTHOR CONTRIBUTIONS

PR led the overall effort. EB, VB, PB, AF, DH, AJL, AL, RM, MM, PO, DP, ES, RS, NT, PY, and BZ were members of the science team and/or provided input into the mission concept. MD, BF, KF, TG, JH, JO and MT were involved in the design of the instruments, spacecraft, and mission. AB and CF led the simulation efforts.

FUNDING

All authors' institutions provided the resources necessary to complete this work.

REFERENCES

Abbott, B. P., Abbott, R., Abbott, T. D., Abernathy, M. R., Acernese, F., Ackley, K., et al. (2016). Astrophysical implications of the binary black-hole merger GW150914. *Astrophys. J. Lett*. 818:22. doi: 10.3847/2041-8205/818/2/L22

Abbott, B. P., Abbott, R., Abbott, T. D., Acernese, F., Ackley, K., Adams, C., et al. (2017). Multi-messenger observations of a binary neutron star merger. *Astrophys. J. Lett*. 848:12. doi: 10.3847/2041-8213/aa91c9

Ahn, K., Iliev, I., Shapiro, P. R., Mellema, G., Koda, J., and Mao, Y. (2012). Detecting the rise and fall of the first stars by their impact on cosmic reionization. *Astrophys. J. Lett*. 756:L16. doi: 10.1088/2041-8205/756/1/L16

Alexander, K. D., Berger, E., Fong, W., Williams, P. K. G., Guidorzi, C., Margutti, R., et al. (2017). The electromagnetic counterpart of the binary neutron star merger ligo/virgo gw170817. VI. Radio constraints on a relativistic jet and predictions for late-time emission from the kilonova ejecta. *Astrophys. J. Lett*. 848:21. doi: 10.3847/2041-8213/aa905d

Alvarez, M., Bromm, V., and Shapiro, P. R. (2006). The H II region of the first star. *Astrophys. J.* 639, 621–632. doi: 10.1086/499578

Amati, L., O'Brien, P., Götz, D., Bozzo, E., Tenzer, C., Frontera, F., et al. (2018). The THESEUS space mission concept: science case, design and expected performances. *Adv. Space Res.* 62, 191–244. doi: 10.1016/j.asr.2018.03.010

Angel, J. R. P. (1979). Lobster eyes as X-Ray telescopes. *Astrophys. J.* 233, 364–373. doi: 10.1086/157397

Baron, E., Branch, D., Hauschildt, P. H., Filippenko, A. V., Kirshner, R. P., Challis, P. M., et al. (2000). Preliminary spectral analysis of the type II supernova 1999em. *Astrophys. J.* 545, 444–448. doi: 10.1086/317795

Barthelmy, S. D., Barbier, L. M., Cummings, J. R., Fenimore, E. E., Gehrels, N., Hullinger, D., et al. (2005). The burst alert telescope (BAT) on the Swift Midex Mission. *Space Sci. Rev*. 120, 143–164. doi: 10.1007/s11214-005-5096-3

Bayless, A. J., Fryer, C. L., Wollaeger, R., Wiggins, B., Even, W., de la Rosa, J., et al. (2017). The supernovae analysis application (SNAP). *Astrophys. J.* 846:101. doi: 10.3847/1538-4357/aa831d

Belczynski, K., Buonanno, A., Cantiello, M., Fryer, C. L., Holz, D. E., Mandel, I., et al. (2014). The formation and gravitational-wave detection of massive stellar black hole binaries. *Astrophys. J.* 789:120. doi: 10.1088/0004-637X/789/2/120

Beletic, J. W., Blank, R., Gulbransen, D., Lee, D., Loose, M., Piquette, E. C., et al. (2008). Teledyne imaging sensors: infrared imaging technologies for astronomy and civil space. *Proc. Soc. Photo-Opt. Ins*. 7021:14. doi: 10.1117/12.790382

Bromm, V. (2013). Formation of the first stars. *Rep. Prog. Phys*. 76:112901. doi: 10.1088/0034-4885/76/11/112901

Bromm, V., and Loeb, A. (2006). High-redshift gamma-ray bursts from population? iii progenitors. *Astrophys. J.* 642, 382–388. doi: 10.1086/500799

Brown, P. J., Breeveld, A. A., Holland, S., Kuin, P., and Pritchard, T. (2014). SOUSA: the swift optical/ultraviolet supernova archive. *Astrophys. J. Suppl. S* 354, 89–96. doi: 10.1007/s10509-014-2059-8

Brown, P. J., Roming, P. W. A., and Milne, P. A. (2015). The first ten years of Swift supernovae. *J. High Energy Astrophys*. 7, 111–116. doi: 10.1016/j.jheap.2015.04.007

Burrows, D. N., Fox, D., Palmer, D., Romano, P., Mangano, V., La Parola, V., et al. (2012). Optimizing the search for high-z GRBs: the JANUS X-ray coded aperture telescope. *Mem. Soc. Astron. Ital. Suppl*. 21:59.

Campana, S., Mangano, V., Blustin, A. J., Brown, P., Burrows, D. N., Chincarini, G., et al. (2006) The association of GRB 060218 with a supernova and the evolution of the shock wave. *Nature* 443, 1008–1010. doi: 10.1038/nature04892

Cardelli, J. A., Clayton, G. C., and Mathis, J. S. (1989). The relationship between infrared, optical, and ultraviolet extinction. *Astrophys. J.* 345, 245–256.

Chornock, R., Berger, E., Fox, D. B., Lunnan, R., Drout, M. R., Fong, W. F., et al. (2013). GRB 130606a as a probe of the intergalactic medium and the interstellar mediumin a star-forming galaxy in the first gyr after the big bang. *Astrophys. J.* 774:26. doi: 10.1088/0004-637X/774/1/26

Chornock, R., Berger, E., Kasen, D., Cowperthwaite, P. S., Nicholl, M., Villar, V. A., et al. (2017). The electromagnetic counterpart of the binary neutron star merger ligo/virgo gw170817. iv. detection of near-infrared signatures of *r*-process nucleosynthesis with gemini-south. *Astrophys. J. Lett*. 848:19. doi: 10.3847/2041-8213/aa905c

de la Rosa, J., Roming, P., Pritchard, T., and Fryer, C. (2016). Characterizing mid-ultraviolet to optical light curves of nearby type iin supernovae. *Astrophys. J.* 820:74. doi: 10.3847/0004-637X/820/1/74

Döhring, T., Jedamzik, R., Westerhoff, T., and Hartmann, P. (2009). Four decades of ZERODUR mirror substrates for astronomy. *Proc. Soc. Photo-Opt. Ins*. 7281:728103. doi: 10.1117/12.831423

Dominik, M., Belczynski, K., Fryer, C., Holz, D. E., Berti, E., Bulik, T., et al. (2015). Double compact objects. III. Gravitational-wave detection rates. *Astrophys. J.* 806:263. doi: 10.1088/0004-637X/806/2/263

Dorn, R. J., Eschbaumer, S., Finger, G., Ives, D., Meyer, M., and Stegmeier, J. (2008). Evaluation of the teledyne SIDECAR ASIC at cryogenic temperature using a visible hybrid H2RG focal plane array in 32 channel readout mode. *Proc. Soc. Photo-Opt. Ins*. 7742, 774219. doi: 10.1117/12.856643

Evans, P. A., Cenko, S. B., Kennea, J. A., Emery, S. W. K., Kuin, N. P. M., Korobkin, O., et al. (2017). Swift and NuSTAR observations of GW170817: detection of a blue kilonova. *Science* 358, 1565–1570. doi: 10.1126/science.aap9580

Evans, P. A., Willingale, R., Osborne, J. P., O'Brien, P. T., Page, K. L., Markwardt, C. B., et al. (2010). The swift burst analyser i: bat and xrt spectral and flux evolution of gamma ray bursts. *Astron. Astrophys*. 519:A102. doi: 10.1051/0004-6361/201014819

Falk, S. (1978). Shock steepening and prompt thermal emission in supernova. *Astrophys. J. Lett*. 225, 133–136.

Fialkov, A., and Loeb, A. (2017). Jetted tidal disruptions of stars as a flag of intermediate mass black holes at high redshifts. *Mon. Not. R. Astron. Soc*. 471, 4286–4299. doi: 10.1093/mnras/stx1755

Fleming, B. T., McCandliss, S. R., Redwine, K., Kaiser, M. E., Kruk, J., Feldman, P. D., et al. (2013). Calibration and flight qualification of FORTIS. *Proc. Soc. Photo-Opt. Ins*. 8859:88590. doi: 10.1117/12.2024189

France, K., McCandliss, S. R., Burgh, E. B., and Feldman, P. D. (2004). Rocket and *Far Ultraviolet Spectroscopic Explorer* Observations of IC 405: differential extinction and fluorescent molecular hydrogen. *Astrophys. J.* 616, 257–265. doi: 10.1086/424813

France, K., Parke Loyd, R. O., Youngblood, A., Brown, A., Schneider, P. C., Hawley, S. L., et al. (2016). The MUSCLES treasury survey. I. motivation and overview. *Astrophys. J.* 820:89. doi: 10.3847/0004-637X/820/2/89

Fraser, G. W., Brunton, A. N., Bannister, N. P., Pearson, J. F., Ward, M., Stevenson, T. J., et al. (2002). LOBSTER-ISS: an imaging x-ray all-sky monitor for the International Space Station. *Proc. Soc. Photo-Opt. Ins*. 4497, 115–126. doi: 10.1117/12.454217

Fraser, G. W., Carpenter, J. D., Rothery, D. A., Pearson, J. F., Martindale, A., Huovelin, J., et al. (2010). The mercury imaging X-ray spectrometer (MIXS) on bepicolombo. *Planet. Space Sci*. 58, 79–95. doi: 10.1016/j.pss.2009.05.004

Fryer, C., Woosley, S., and Hartmann, D. (1999). Formation rates of black hole accretion disk gamma-ray bursts. *Astrophys. J.* 526, 152–177.

Fryer, C. L., Belczynski, K., Ramirez-Ruiz, E., Rosswog, S., Shen, G., and Steiner, A. W. (2015). The fate of the compact remnant in neutron star mergers *Astrophys. J.* 812:24. doi: 10.1088/0004-637X/812/1/24

Gardner, J. P., Mather, J. C., Clampin, M., Doyon, R., Greenhouse, M. A., Hammel, H. B., et al. (2006). The james webb space telescope. *Space Sci. Rev.* 123, 485–606. doi: 10.1007/s11214-006-8315-7

Garnavich, P. M., Tucker, B. E., Rest, A., Shaya, E. J., Olling, R. P., Kasen, D., et al. (2016). Shock breakout and early light curves of type ii-p supernovae observed withkepler. *Astrophys. J.* 820:23. doi: 10.3847/0004-637X/820/1/23

Gehrels, N., Chincarini, G., Giommi, P., Mason, K. O., Nousek, J. A., Wells, A. A., et al. (2004). The *Swift* gamma-ray burst mission. *Astrophys. J.* 611, 1005–1020. doi: 10.1086/422091

Gehrels, N., and Razzaque, S. (2013). Gamma-ray bursts in the swift-Fermi era. *Front. Phys.* 8, 661–678. doi: 10.1007/s11467-013-0282-3

Gezari, S., Dessart, L., Basa, S., Martin, D. C., Neill, J. D., Woosley, S. E., et al. (2008). Probing shock breakout with serendipitous *galex* detections of two snls type ii-p supernovae. *Astrophys. J. Lett.* 683:131. doi: 10.1086/591647

Goldstein, A., Veres, P., Burns, E., Briggs, M. S., Hamburg, R., Kocevski, D., et al. (2017). An ordinary short gamma-ray burst with extraordinary implications: *Fermi*-GBM detection of GRB 170817A. *Astrophys. J. Lett.* 848:14. doi: 10.3847/2041-8213/aa8f41

Haggard, D., Nynka, M., Ruan, J. J., Kalogera, V., Cenko, S. B., Evans, P., et al. (2017). A deep *Chandra* X-Ray study of neutron star coalescence GW170817. *Astrophys. J. Lett.* 848:L25. doi: 10.3847/2041-8213/aa8ede

Hallinan, G., Corsi, A., Mooley, K. P., Hotokezaka, K., Nakar, E., Kasliwal, M. M., et al. (2017). A radio counterpart to a neutron star merger. *Science* 358, 1579–1583. doi: 10.1126/science.aap9855

Harman, C. E., Schwieterman, E. W., Schottelkotte, J. C., and Kasting, J. F. (2015). Abiotic O_2 levels on planets around f, g, k, and m stars: possible false positives for life? *Astrophys. J.* 812:137. doi: 10.1088/0004-637X/812/2/137

Hartoog, O. E., Malesani, D., Fynbo, J. P. U., Goto, T., Krühler, T., Vreeswijk, P. M., et al. (2015). VLT/X-shooter spectroscopy of the afterglow of the swift GRB 130606A - chemical abundances and reionisation at z $\sim$ 6. *Astron. Astrophys.* 580:A139. doi: 10.1051/0004-6361/201425001

Höflich, P., and Schaefer, B. E. (2009). X-ray and gamma-ray flashes from type Ia supernovae? *Astrophys. J.* 705, 483–495. doi: 10.1088/0004-680637X/705/1/483

Hu, R., Seager, S., and Bains, W. (2012). Photochemistry in terrestrial exoplanet atmospheres. i. photochemistry model and benchmark cases. *Astrophys. J.* 761:166. doi: 10.1088/0004-637X/761/2/166

Ioka, K., Suwa, Y., Nagakura, H., de Souza, R. S., and Yoshida, N. (2012). Population III gamma-ray burst. *Int. Astron. Union Symp.* 279, 301–304. doi: 10.1017/S1743921312013099

Jakobsson, P., Hjorth, J., Malesani, D., Chapman, R., Fynbo, J. P. U., Tanvir, N. R., et al. (2012). The optically unbiased GRB host (TOUGH) survey. III. Redshift distribution *Astrophys. J.* 752:62. doi: 10.1088/0004-637X/752/1/62

Johnson, J. L., Whalen, D. J., Fryer, C. L., and Li, H. (2012). On the formation of the first quasars. *Astrophys. J.* 750:66. doi: 10.1088/0004-637X/750/1/66

Kasen, D. (2010). Seeing the collision of a supernova with its companion star *Astrophys. J.* 708, 1025–1031. doi: 10.1088/0004-637X/708/2/1025

Kasen, D., Fernández, R., and Metzger, B. D. (2015). Kilonova light curves from the disk wind outflows of compact object mergers. *Mon. Not. R. Astron. Soc.* 450, 1777–1786. doi: 10.1093/mnras/stv721

Kasliwal, M. M., Nakar, E., Singer, L. P., Kaplan, D. L., Cook, D. O., Van Sistine, A., et al. (2017). Illuminating gravitational waves: a concordant picture of photons from a neutron star merger. *Science* 358:6370.doi: 10.1126/science.aap9455

Kennea, J. A. (2015). The galactic transient sky with swift *J. High Energy Astrophys.* 7, 105–110. doi: 10.1016/j.jheap.2015.03.006

Kisaka, S., Ioka, K., and Nakar, E. (2016). X-ray-powered macronovae. *Astrophys. J.* 818:104. doi: 10.3847/0004-637X/818/2/104

Klein, R., and Chevalier, R. (1978). X-ray bursts from type II supernovae. *Astrophys. J. Lett.* 223, 109–112. doi: 10.1086/182740

Lopez, L. A., Grefenstette, B. W., Reynolds, S. P., An, H., Boggs, S. E., Christensen, F. E., et al. (2015). A spatially resolved study of the synchrotron emission and titanium in tychossupernova remnant usingnustar. *Astrophys. J.* 814:132. doi: 10.1088/0004-637X/814/2/132

Lupu, R. E., McCandliss, S. R., Fleming, B., France, K., Feldman, P. D., and Nikzad, S. (2008). Calibration and flight performance of the long-slit imaging dual order spectrograph. *Proc. Soc. Photo-Opt. Ins.* 7011:70113I. doi: 10.1117/12.786435

Maoz, D., Mannucci, F., and Nelemans, G. (2014). Observational clues to the progenitors of type Ia supernovae. *Annu. Rev. Astron. Astrophys.* 52, 107–170. doi: 10.1146/annurev-astro-082812-141031

Margutti, R., Berger, E., Fong, W., Guidorzi, C., Alexander, K. D., Metzger, B. D., et al. (2017). The Electromagnetic counterpart of the binary neutron star merger LIGO/Virgo GW170817. V. rising x-ray emission from an off-axis jet. *Astrophys. J. Lett.* 848:20. doi: 10.3847/2041-8213/aa9057

Matzner, C. D., and McKee, C. F. (1999). The expulsion of stellar envelopes in core-collapse supernovae. *Astrophys. J.* 510, 379–403. doi: 10.1086/306571

Mercier, K., Gonzalez, F., Jouret-Perl, M., Atteia, J. L., Mandrou, P., Pons, R., et al. (2014). The french payload on-board the SVOM french-chinese mission. *Proc. Soc. Photo-Opt. Ins.* 9144:914422. doi: 10.1117/12.2055163

Mészáros, P., and Rees, M. J. (2010). Population III gamma ray bursts. *Astrophys. J.* 715, 967–971. doi: 10.1088/0004-637X/715/2/967

Metzger, B. D. (2017). Living reviews in relativity: kilonovae by brian D. metzger living. *Rev. Relativ.* 20:3. doi: 10.1007/s41114-017-0006-z

Modjaz, M., Li, W., Butler, N., Chornock, R., Perley, D., Blondin, S., et al. (2009). From shock breakout to peak and beyond: extensive panchromatic observations ofthe type ib supernova 2008d associated withswiftx-ray transient 080109. *Astrophys. J.* 702, 226–248. doi: 10.1088/0004-637X/702/1/226

Nakar, E., and Sari, R. (2010). Early supernovae light curves following the shock breakout. *Astrophys. J.* 725, 904–921. doi: 10.1088/0004-637X/725/1/904

Nicholl, M., Berger, E., Kasen, D., Metzger, B. D., Elias, J., Briceño, C., et al. (2017). The electromagnetic counterpart of the binary neutron star merger LIGO/Virgo GW170817. III. Optical and UV spectra of a blue kilonova from fast polar ejecta. *Astrophys. J. Lett.* 848:18. doi: 10.3847/2041-8213/aa9029

Osborne, J. P., O'Brien, P., Evans, P., Fraser, G. W., Martindale, A., Atteia, J. L., et al. (2013). A-STAR: the all-sky transient astrophysics reporter. *EAS Publications* 61, 625–631. doi: 10.1051/eas/1361099

Park, S., Roming, P. W. A., Hughes, J. P., Slane, P. O., Burrows, D. N., Garmire, G. P., et al. (2002). The structure of the oxygen-rich supernova remnant g292.0+1.8 from *chandra* X-ray images: shocked ejecta and circumstellar medium. *Astrophys. J. Lett.* 564, 39–43. doi: 10.1086/338861

Pian, E., D'Avanzo, P., Benetti, S., Branchesi, M., Brocato, E., Campana, S., et al. (2017). Spectroscopic identification of r-process nucleosynthesis in a double neutron-star merger. *Nature* 551, 67–70. doi: 10.1038/nature24298

Piro, A. L., Chang, P., and Weinberg, N. N. (2010). Shock breakout from type Ia supernova. *Astrophys. J.* 708, 598–604. doi: 10.1088/0004-637X/708/1/598

Predehl, P., and Schmitt, J. H. M. M. (1995). X-raying the interstellar medium: ROSAT observations of dust scattering halos. *Astron. Astrophys.* 293, 889–905.

Pritchard, T. A., Roming, P. W. A., Brown, P. J., Bayless, A. J., and Frey, L. H. (2014). Bolometric AND UV light curves of core-collapse supernovae. *Astrophys. J.* 787:157. doi: 10.1088/0004-637X/787/2/157

Raab, W., Branduardi-Raymont, G., Wang, C., Dai, L., Donovan, E., Enno, G., et al. (2016). SMILE: a joint ESA/CAS mission to investigate the interaction between the solar wind and Earth's magnetosphere. *Proc. Soc. Photo-Opt. Ins.* 9905:990502. doi: 10.1117/12.2231984

Regimbau, T., Siellez, K., Meacher, D., Gendre, B., and Boër, M. (2015). Revisiting coincidence rate between gravitational wave detection and short gamma-ray burst for the advanced and third generation. *Astrophys. J.* 799:69R. doi: 10.1088/0004-637X/799/1/69

Robertson, B. E., Ellis, R. S., Furlanetto, S. R., and Dunlop, J. S. (2015). Cosmic reionization and early star-forming galaxies: a joint analysis of new constraints from planck and the hubble space telescope *Astrophys. J. Lett.* 802:L19. doi: 10.1088/2041-8205/802/2/L19

Roming, P. W. A., Bilén, S. G., Burrows, D. N., Falcone, A. D., Fox, D. B., Herter, T. L., et al. (2012). Joint astrophysics nascent universe satellite: utilizing GRBs as high redshift probes. *Mem. Soc. Astron. Ital. Suppl.* 21, 155–161.

Roming, P. W. A., Kennedy, T. E., Mason, K. O., Nousek, J. A., Ahr, L., Bingham, R. E., et al. (2005). The swift ultra-violet/optical telescope. *Space Sci. Rev.* 120, 95–142. doi: 10.1007/s11214-005-5095-4

Roming, P. W. A., Koch, T. S., Oates, S. R., Porterfield, B. L., Vanden Berk, D. E., Boyd, P. T., et al. (2009). The first swift ultra-violet/optical telescope grb afterglow catalog. *Astrophys. J.* 690, 163–188. doi: 10.1088/0004-637X/690/1/163

Seager, S., Bains, W., and Hu, R. (2013). Biosignature gases in h2-dominated atmospheres on rocky exoplanets. *Astrophys. J.* 777:95. doi: 10.1088/0004-637X/777/2/95

Shkolnik, E. L., and Barman, T. S. (2014). Hazmat. I. THE evolution of far-uv and near-uv emission from early m stars. *Astron. J.* 148:64. doi: 10.1088/0004-6256/148/4/64

Smartt, S. J. (2009). Progenitors of core-collapse supernovae. *Annu. Rev. Astron. Astrophys.* 47, 63–106. doi: 10.1146/annurev-astro-082708-101737

Smartt, S. J., Chen, T. W., Jerkstrand, A., Coughlin, M., Kankare, E., Sim, S. A., et al. (2017). A kilonova as the electromagnetic counterpart to a gravitational-wave source. *Nature* 551, 75–79. doi: 10.1038/nature24303

Soderberg, A. M., Berger, E., Page, K. L., Schady, P., Parrent, J., Pooley, D., et al. (2008). An extremely luminous X-ray outburst at the birth of a supernova. *Nature* 453, 469–474. doi: 10.1038/nature06997

Spake, J. J., Sing, D. K., Evans, T. M., Oklopčić, A., Bourrier, V., Kreidberg, L., et al. (2018). Helium in the eroding atmosphere of an exoplanet. *Nature* 557, 68–70. doi: 10.1038/s41586-018-0067-5

Spergel, D., Gehrels, N., Baltay, C., Bennett, D., Breckinridge, J., Donahue, M., et al. (2015). Wide-Field InfraRed Survey Telescope - Astrophysics Focused Telescope Assets WFIRST-AFTA 2015 report. eprint *arXiv [Preprint]. arXiv:*1503.03757.

Strolger, L. G., Dahlen, T., Rodney, S. A., Graur, O., Riess, A. G., McCully, C., et al. (2015). The rate of core collapse supernovae to redshift 2.5 from the CANDELS and CLASH supernova surveys. *Astrophys. J.* 813:93. doi: 10.1088/0004-637X/813/2/93

Sun, H., Zhang, B., and Gao, H. (2017). X-ray counterpart of gravitational waves due to binary neutron star mergers: light curves, luminosity function, and event rate density. *Astrophys. J.* 835:7. doi: 10.3847/1538-4357/835/1/7

Tanaka, M. (2016). Kilonova/macronova emission from compact binary mergers. *Adv. Astron.* 2016:6341974. doi: 10.1155/2016/6341974

Tanvir, N. R., and Jakobsson, P. (2007). Observations of GRBs at high redshift. *Philos. Trans. R. Soc. A* 365, 1377–1384. doi: 10.1098/rsta.2006.1992

Tanvir, N. R., Levan, A. J., Fruchter, A. S., Fynbo, J. P. U., Hjorth, J., Wiersema, K., et al. (2012). Star formation in the early universe: beyond the tip of the iceberg. *Astrophys. J.* 754:46. doi: 10.1088/0004-637X/754/1/46

Tanvir, N. R., Levan, A. J., González-Fernández, C., et al. (2017). The emergence of a lanthanide-rich kilonova following the merger of two neutron stars. *Astrophys. J.* 848:L27. doi: 10.3847/2041-8213/aa90b6

Tian, F., France, K., Linsky, J. L., Mauas, P. J. D., and Vieytes, M. C. (2014). High stellar FUV/NUV ratio and oxygen contents in the atmospheres of potentially habitable planets. *Earth Planet Sci. Lett.* 385, 22–27. doi: 10.1016/j.epsl.2013.10.024

Totani, T., Kawai, N., Kosugi, G., Aoki, K., Yamada, T., Iye, M., et al. (2006). Implications for cosmic reionization from the optical afterglow spectrum of the gamma-ray burst 050904 at z = 6.3. *Publ. Astron. Soc. Jpn.* 58, 485–498. doi: 10.1093/pasj/58.3.485

Troja, E., Piro, L., van Eerten, H., Wollaeger, R. T., Im, M., Fox, O. D., et al. (2017). The X-ray counterpart to the gravitational-wave event GW170817. *Nature* 551, 71–74. doi: 10.1038/nature24290

Wanderman, D., and Piran, T. (2010). The luminosity function and the rate of *Swift's* gamma-ray bursts. *Mon. Not. R. Astron. Soc.* 406, 1944–1958. doi: 10.1111/j.1365-2966.2010.16787.x

Wang, B., and Han, Z. (2012). Progenitors of type Ia supernovae. *New Astron. Rev.* 56, 122–141. doi: 10.1016/j.newar.2012.04.001

Whalen, D., and Fryer, C. (2012). The formation of supermassive black holes from low-mass pop III seeds. *Astrophys. J. Lett.* 756:L19. doi: 10.1088/2041-8205/756/1/L19

White, D. J., Daw, E. J., and Dhillon, V. S. (2011). A list of galaxies for gravitational wave searches. *Class. Quant. Grav.* 28:085016. doi: 10.1088/0264-9381/28/8/085016

Willingale, R., Starling, R. L. C., Beardmore, A. P., Tanvir, N. R., and O'Brien, P. T. (2010). Calibration of X-ray absorption in our Galaxy. *Mon. Not. R. Astron. Soc.* 431, 394–404. doi: 10.1093/mnras/stt175

Wootten, A., and Thompson, A. R. (2009). The atacama large millimeter/submillimeter array. *Proc. IEEE* 97, 1463–1471. doi: 10.1109/JPROC.2009.2020572

Zhang, B. (2013). Early X-ray and optical afterglow of gravitational wave bursts from mergers of binary neutron stars. *Astrophys. J. Lett.* 763:22. doi: 10.1088/2041-8205/763/1/L22

Conflict of Interest Statement: The authors declare that the research was conducted in the absence of any commercial or financial relationships that could be construed as a potential conflict of interest.